RSC Advances

PAPER

View Article Online
View Journal | View Issue

Cite this: *RSC Adv.*, 2022, **12**, 33429

Catalytic ozonation of dichloromethane at low temperature and even room temperature on Mn-loaded catalysts†

Yaxin Duan,[a] Peixi Liu,[a] Fawei Lin,[b] Yong He,[a] Yanqun Zhu[a] and Zhihua Wang *[a]

Five Mn-loaded catalysts were synthesized on γ-Al_2O_3, TiO_2, ZrO_2, nano γ-Al_2O_3 and nanoZrO_2 supports. The catalytic ozonation of DCM (dichloromethane) was evaluated under industrial conditions (*i.e.*, temperature, O_3 input, H_2O and SO_2 content). According to results, >90% DCM conversion without O_3 residue was achieved for all samples at 120 °C and an O_3/DCM ratio of 6. At 20–120 °C, the highest Mn^{3+} content, abundant surface oxygen species and more weak acid sites led to the best performance of Mn/nanoAl_2O_3 (M/A-II). At 20 °C and 120 °C, 80% and 95% DCM can be degraded respectively on M/A-II at 20 °C with matched surface oxygen species and acidity. An O_3/DCM ratio of 6 was optimal for performance and economy. For the effects of complex exhaust, both H_2O and SO_2 deactivated M/A-II. The H_2O-induced deactivation was recoverable and also removed surface-deposited chlorine-containing species, enhancing the HCl selectivity. Finally, the Cl equilibrium of the reaction was comprehensively analyzed.

Received 15th September 2022
Accepted 14th November 2022

DOI: 10.1039/d2ra05828f

rsc.li/rsc-advances

1. Introduction

Achieving sustainable green and low-carbon development requires the secondary utilization of waste (*e.g.*, upgrading waste plastics to arenes,[1] using biomass to produce organo-nitrogen chemicals[2]) and the reduction of polluting waste (including solid, liquid and gaseous) emissions. Simultaneously, the control of pollutants can also lessen the pressure of waste utilization and conversion. As highly toxic and hard to degrade organic gas pollutants, chlorinated VOCs deserve attention. As a typical species of chlorinated VOCs, dichloromethane (DCM, CH_2Cl_2) has been identified as priority pollutant for strict control in the US, EU, and China.[3] Due to its exceptional organic solubility, DCM has been frequently used in painting,[4] chemical synthesis pharmaceuticals,[5] synthetic resin[6] *etc.* According to studies, direct exposure and accumulation of highly toxic DCM[7,8] can cause central nervous system damage, cancer, and even genetic mutations.[5,9] DCM emitting into atmosphere will result in photochemical smog and aerosols, as well as forming more powerful radicals that deplete stratospheric ozone.[10] Hence, DCM degradation is an urgent issue to be addressed. Catalytic degradation is the dominant (when DCM < 1000 ppm) destructive technology because of its high degradation rate, low costs, and products controllability.

Most research use noble metals and transition metals as DCM catalysts. The noble metals, *i.e.*, Rh, Ru, Pt, and Pd, are usually loaded on a single or synthetic supports such as TiO_2, Al_2O_3, CeO_2, SiO_2, HZSM-5, Ti_xSn_{1-x}, *etc.*[11–15] The improved dispersion and formation of ligand bonds between noble metals and supports allowed for efficient DCM degradation. Ru exhibits better capabilities among all these noble metals, while PCDD/Fs-containing by-products was inevitable.[13] Transition metals oxides possess multiple valence states, stronger interactions with appropriate others, and better resistance to chlorine-containing species for DCM degradation. Constantly emerging materials with desired catalytic properties include Nb-CeNTs,[16] X_4/TiO_2 (X = V, Ce, Mn),[17] Ce/TiO_2.[18] However, the T_{90} (temperature required to convert 90% DCM) of above catalysts were generally above 400 °C. To obtain high degradation rates at lower temperatures, several catalyst modification attempts had been made.[19–23] For example, Wang *et al.* reported that spinel-type $CoCr_2O_4$ with high specific surface area prepared by sol–gel method declined T_{90} of DCM conversion to 257 °C.[21] Xia *et al.* investigated the effect of sulphating treatment on the iron titanate catalysts, which attained T_{90} of DCM conversion declining from 300 °C to 250 °C.[22] However, the lowest T_{90} of DCM conversion over catalysts with transition metals was reported to be ~200 °C.[23]

Recently, it has become appealing to employ active molecule O_3 in conjunction with simpler and cheaper catalysts for pollutants degradation. In comparison with conventional catalytic oxidation, O_3 can further lower the activation energy of

[a]*State Key Laboratory of Clean Energy Utilization, Zhejiang University, Hangzhou 310027, P. R. China. E-mail: wangzh@zju.edu.cn; Tel: +86-0571-879531*

[b]*School of Environmental Science and Engineering, Tianjin University, Tianjin 300072, P. R. China*

† Electronic supplementary information (ESI) available. See DOI: https://doi.org/10.1039/d2ra05828f

VOCs oxidation, allowing effective VOCs degradation at temperatures below 200 °C or even at ambient temperature,[24] and facilitating catalyst stability.[25] Ozone decomposition increases the quantity of high-valent metal ions and reactive oxygen species (*e.g.*, $-O_2$ and –OH) on the catalyst surface, contributing to deeper oxidation and increased activity.[26] Among a series of transition metals, O_3 typically performs well over Mn-based catalysts, effectively degrading compounds such as NO,[27] formaldehyde,[28] benzene,[29] toluene,[30] and chlorobenzene.[31,32] However, seldom studies focused on catalytic ozonation of DCM.[33] Generally, low-temperature DCM oxidation over Mn-based catalysts usually exhibits poor performance. Low DCM conversion, negligible mineralization rate, and Cl_2 poisoning of the catalyst due to the active Deacon reaction are commonly reported[17,34,35] as well as lacking considering real industry conditions. Supported catalysts with large surface area and matched surface acidity and redox ability are good choices for catalytic ozonation of DCM. Therefore, it is worthwhile to explore the O_3 coupling of Mn-loaded catalysts to achieve DCM degradation under reality conditions.

Herein, Mn-loaded catalysts were prepared on industrially common supports (γ-Al_2O_3, TiO_2, ZrO_2) using an evaporation–drying impregnation method. Nano γ-Al_2O_3 and nano ZrO_2 supports were also selected to evaluate the effect of metal dispersion on catalytic behaviours. Firstly, catalytic ozonation of DCM over five Mn-loaded catalysts with selectivity of target products and by-products were investigated at temperature of 20–120 °C. Next, the stability and byproducts of the best-performing catalysts in DCM degradation at 120 °C was evaluated in deep. The effects of H_2O and SO_2 on catalytic ozonation of DCM are investigated. Finally, the visible Cl equilibrium of the DCM conversion was evaluated.

2. Experimental methodologies

2.1 Catalyst preparation

In the present experiment, manganese based catalysts were prepared by impregnation method in the present experiment. Unpretreated γ-Al_2O_3, nano γ-Al_2O_3, TiO_2, ZrO_2, and nano ZrO_2 (AR, Aladdin) were used as supports. Around 4 wt% of $Mn(CH_3COO)_2$ (AR, 98%, Aladdin) and 3 g support powder was added successively in 30 mL ethanol solution. After stirring at 800 rpm for 1 h at room temperature, the mixture was stirred in a water bath at 60 °C with suitable speed until nearly dry. The nearly dry samples were moved to the quartz boat and baked at 110 °C for 12 h. The solid was calcined at 450 °C for 3 h under static air atmosphere, following by grinding and sieving into 40 to 60 meshes. Corresponding to the order of above 5 supports, the obtained catalysts are named as M/A-I, M/A-II, M/T, M/Z-I, M/Z-II.

2.2 Experimental setup and activity measurement

The 0.1 g prepared catalyst mixed with suitable amount of quartz sand (40–60 mesh) were loaded in the reactor with a total gas volume of 250 mL min^{-1} (10% O_3/O_2, 100 ppm DCM and equilibrium gas N_2) to maintain a constant gas hourly space velocity (GHSV) around 30 000 h^{-1}. The mole ratio of O_3/DCM was controlled between 1.5 and 8 (Fig. 1).

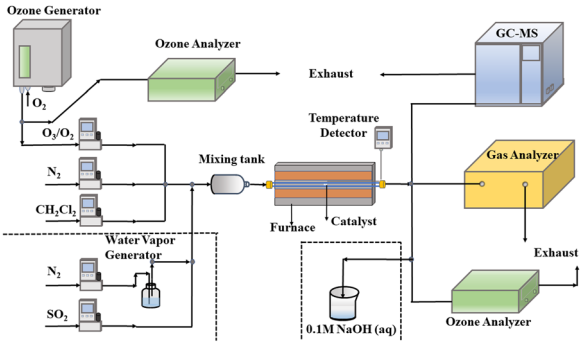

Fig. 1 The diagram of the DCM activity testing test system.

The concentrations of DCM, HCl, $CHCl_3$, CH_3Cl, CHOH and other byproducts from outlet were determined by FT-IR flue gas analyzer (Gasmet FTIR DX4000, Finland). The CO and CO_2 in the off gas were first converted into CH_4 and then analyzed by FID detector in an online gas chromatograph (GC9790-II, Zhejiang Fuli Co., Ltd). The ozone residue was measured by a low concentration ozone analyzer (BMT-932-1, OSTI Inc.; 0–100 ppm, ±0.1 ppm). In particular, the Cl_2 was absorbed in 30 mL NaOH solution (0.01 M) within fixed time (*e.g.* one minute), and the solution was determined by residual chlorine concentration meter (1 mg L^{-1}, Hana, HI93701). According to eqn (1), the concentration of Cl_2 could be obtained ClO^-.

$$Cl_2 + 2NaOH = NaCl + NaClO + H_2O \quad (1)$$

The conversion rate of DCM, the selectivity of HCl, Cl_2, the yield of CO, CO_2, CO_x (*i.e.* the total amount of CO and CO_2), the ratio of C_{in-out} and the ratio of Cl_{in-out} were defined as:

$$Con.(DCM) = [(DCM)_{in} - (DCM)_{out}]/(DCM)_{in} \times 100\% \quad (2)$$

$$Sel.(HCl) = (HCl)_{out}/2/[(DCM)_{in} - (DCM)_{out}] \times 100\% \quad (3)$$

$$Sel.(Cl_2) = (Cl_2)_{out}/[(DCM)_{in} - (DCM)_{out}] \times 100\% \quad (4)$$

$$Yid.(CO) = (CO)_{out}/(DCM)_{in} \times 100\% \quad (5)$$

$$Yid.(CO_2) = (CO_2)_{out}/(DCM)_{in} \times 100\% \quad (6)$$

$$Yid.(CO_x) = [(CO_2)_{out} + (CO)_{out}]/(DCM)_{in} \times 100\% \quad (7)$$

$$Ratio\ of\ C_{in-out} = [(DCM)_{in} - (C)_{out}]/(DCM)_{in-out} \times 100\% \quad (8)$$

$$Ratio\ of\ Cl_{in-out} = [(DCM)_{in} - (Cl)_{out}]/(DCM)_{in-out}/2 \times 100\% \quad (9)$$

where the in and out at subscript refer to the initial and outlet concentrations of reactants or products. The C_{out} and Cl_{out} represent the total concentration of all detected carbon-containing compounds and chlorine-containing compounds in the exhaust, respectively. The concentration unit for DCM, HCl, Cl_2, CO, CO_2, CO_x, C_{out} and Cl_{out} are ppm.

2.3 Catalyst characterization

X-Ray powder diffractometer (XRD) patterns of support bodies and loaded samples were recorded on X'Pert3 Powder-17005730 (PANalytical B.V., Netherlands), using a PIXcel^{1D} all-purpose matrix detector and the Cu Kα radiation at 40 kV and 40 mA with the step size of 0.026° ranging from 10° to 80°. The morphology of the catalyst powder was observed by a scanning electron microscope (SEM, Zeiss Gemini Sigma 300) operated at 3.0 kV. The distribution of elements on catalysts was detected by EDS mapping (Oxford Xplore 50). Transmission electron microscopy (TEM) was carried out on a JEOL JEM 200PLUS. The actual manganese contents on the synthesized catalysts were detected and calculated by plasma emission spectrometer (Aglient 5110) using microwave-dissolved solutions. Nitrogen adsorption–desorption isotherms of catalysts were tested on Quantachrome Autosorb IQ3 adsorption apparatus at 77 K after degasification at 200 °C for 4 h. The specific surface area, average pore size and pore volume of all samples were calculated by Brunauer–Emmett–Teller (BET) or Barrett–Joyner–Halenda (BJH) method. Surface element composition and valence were carried out by X-ray photoelectron spectroscopy (XPS, Thermo Scientific Escalab 250Xi) with Al Kα X-ray settings of 1486.6 eV. The transfer of binding energy for the adventitious carbon was calibrated with C 1s at 284.8 eV in consideration of the charging effect. Nicolet iS50 FT-IR equipped with a liquid nitrogen-cooled MCT/A detector was used in pyridine infrared spectrometry experiments. The redox properties, surface acidity and the desorption properties of O_2 and DCM were tested on an Automatic chemisorption analyzer (Micromeritics AutoChem II 2920). An on-line quadrupole mass spectrometry (Hiden QIC20) was equipped to detect the outlets containing multiple components. In the H_2-TPR test, ~50 mg samples were pretreated in a flow of He (30 mL min^{-1}) at 200 °C for 1 h and cooled to the initial temperature (50 °C). After maintaining for 30–60 minutes, the samples were heated to 800 °C at a ramp rate of 10 °C min^{-1} in a 5 vol% H_2/N_2 flow (30 mL min^{-1}). The H_2 signals were logged by the TCD (thermal conductivity detector). The H_2 consumptions were quantified with reference to the H_2-TPR spectrum of standard CuO. For the NH_3-TPD, O_2-TPD, and DCM-TPD experiments, the pretreated samples were saturated with a 5 vol% NH_3/He flow, a 2 vol% O_2/He flow, and a 0.3 vol% DCM/N_2 flow (all at 30 mL min^{-1}) for 1 h respectively. Subsequently, the respective tests were performed under the same heating conditions as H_2-TPR.

3. Results and discussion

3.1 Catalytic ozonation of DCM over Mn-loaded catalysts

3.1.1 Effect of support type. Catalytic ozonation of DCM was investigated over Mn-loaded catalysts, *i.e.*, M/A-I, M/A-II, M/T, M/Z-I, and M/Z-II, with a function of temperature, *ca.* 20–120 °C, as the results presented in Fig. 2 and the detailed values listed in Table 1. The O_3/DCM molar ratio was fixed to be 6. The ozone residue at the outlet maintained – zero (<0.1 ppm) for all the tested conditions as shown in Fig. 2(a). As displayed in Fig. 2(a), the DCM conversion of M/A-II was the highest from 20 to 120 °C. At 20–100 °C, the DCM conversions of five different catalysts were ranked as M/A-II ≥ M/A-I > M/Z-II ≥ M/Z-I > M/T, indicating the nano catalyst supports were slightly effective than the non-nano ones. In particular, the DCM conversion of M/A-II reached 80% at 20 °C and continued to rise as the temperature increased. While, the other four catalysts showed a decrease in DCM conversion as the temperature elevating from 20 to 60 °C, which should attribute to the by-products generation and will be explained in section 3.1.2. Interestingly, the byproducts decreased and the DCM conversion rebounded at higher temperatures. Therefore, the DCM conversion of all catalysts reached over 90% at 120 °C. Specifically, the highest DCM conversion achieved ~97.69% by M/A-II catalyst. The other catalyst of M/Z-II, M/Z-I, and M/T shows similar performance with efficiency around 90.21% ~92.58%. For O_3-assisted catalytic oxidation at 120 °C, Chen *et al.*[31] obtained ~82% DCM conversion at a O_3/DCM of 10 with Mn/Al_2O_3 catalyst.

For DCM catalytic oxidation by O_2 under the same operating conditions, the DCM conversion of identical samples at 200 °C was less than 10% as shown in Fig. S1,† indicating significant promotion of O_3 on the DCM degradation. Comparing with previous studies, the DCM conversion of catalytic oxidation by O_2 below 300 °C was only 40% over Mn_4/TiO_2 (ref. 17) and less than 10% over 30MnAl.[35] Mn–Co@Z loaded with a dual active component also failed to achieve 50% DCM conversion at 360 °C.[34] Obviously, the addition of ozone can greatly decrease the needed reaction temperature of DCM.

Fig. 2(b) shows the yields of CO and CO_2. The yield of CO_x (*i.e.*, CO + CO_2) was approximately equal to the conversion of DCM, indicating effective DCM-catalyzed ozonation and carbon equilibrium. Overall, the higher CO yield may be caused by the limited deep oxidation at low temperatures especially less than 80 °C.[31] The highest CO_2 yield on M/A-II, reaching 39.18% at 120 °C and results are shown in Table 1, corresponding to the best activity performance, but still lots of CO emitted. Although Xiang *et al.*[33] obtained slightly higher CO_2 yields over 1/8Cu-HU-MnO_2 than those produced here over M/A-II, the same DCM conversion was also obtained at a lower ozone dosage usage of O_3/DCM of 6.

Fig. 2(c) and (d) illustrate the selectivity of HCl and Cl_2 during catalytic ozonation of DCM. Cl_2 was dominant chlorine containing species at low temperature region, *ca.* 20–40 °C. Indicating the O_3 could promote the Deacon reaction (O_3 + 2HCl = H_2O + Cl_2 + O_2) at low temperature transferred HCl into Cl_2.[32] With the elevation of temperature, the HCl selectivity increased slightly.

The O_3 input directly affects the pollutants conversion and products selectivity. Herein, the variation in DCM conversion, HCl, Cl_2, CH_3Cl, and $CHCl_3$ selectivity over M/A-II with increasing molar ratio of O_3/DCM were examined, as the results presented in Fig. 2(e) and (f). Clearly, the DCM conversion continuously increased from ~25% to ~97% as the molar ratio of O_3/DCM rose from 1.5 to 6. Finally, the DCM conversion fluctuated in the range of 97–99% in O_3/DCM of 7–8.

The Cl_2 selectivity was much higher than the HCl selectivity. Although the HCl selectivity increased a little when O_3/DCM

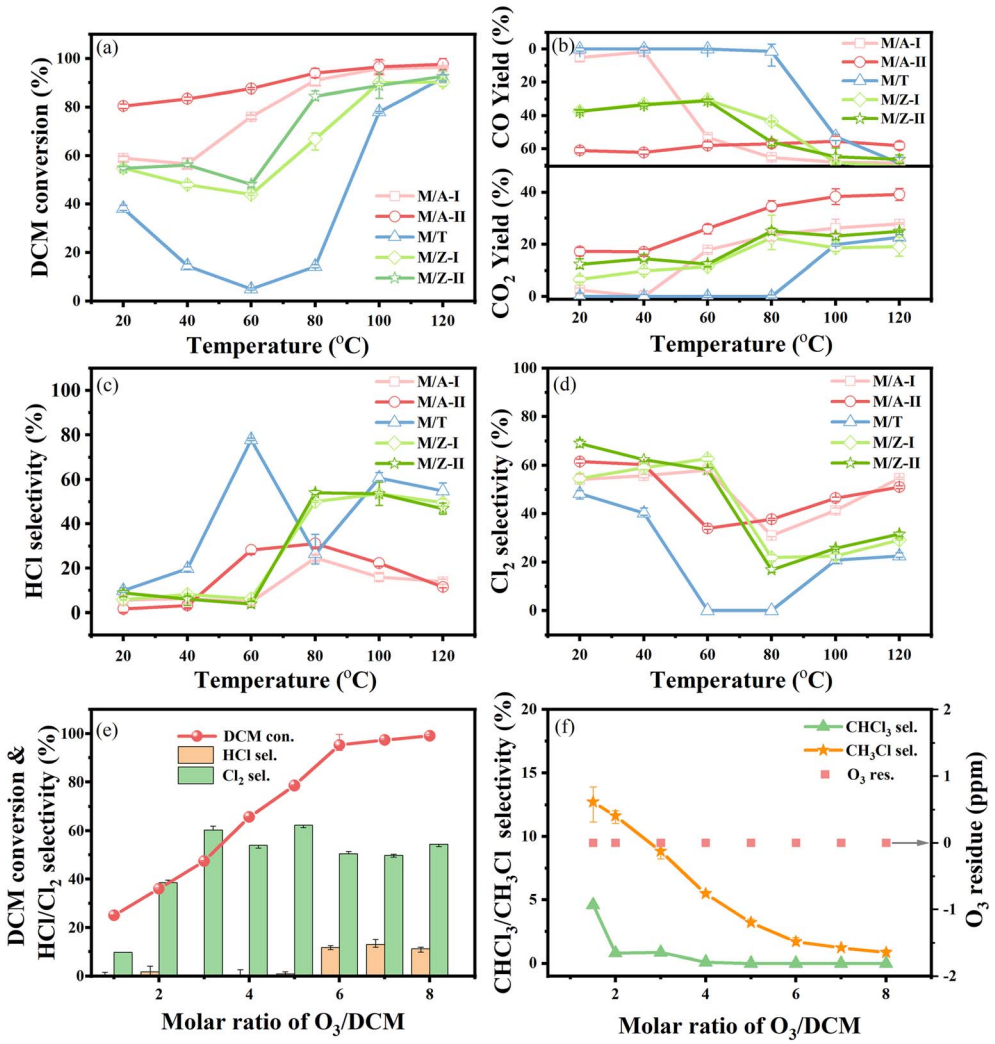

Fig. 2 Catalytic ozonation of DCM over different synthesized catalysts. (a) DCM conversion curve with O_3/DCM of 6 with a function of temperature (20–120 °C); (b) CO and CO_2 yield; (c) and (d) HCl and Cl_2 selectivity. (e) and (f) DCM conversion and chlorinated products at different O_3/DCM molar ratios over M/A-II. (Conditions: GHSV ≈ 30 000 h^{-1}, temperature = 120 °C, DCM initial concentration = 100 ppm, initial molar ratio of O_3/DCM = 1.5–8).

reached 6, the Cl_2 selectivity was still much higher and exhibited more obvious elevation at the initial stage, which indicating that O_3 promoted the Deacon reaction.[31,32] Fig. 2(f) presents that CH_3Cl and $CHCl_3$ both diminish with the increase of O_3/DCM. The $CHCl_3$ selectivity surpassed the CH_3Cl selectivity along the O_3/DCM range, and $CHCl_3$ could not fall to zero even with O_3/DCM of 8. Fortunately, O_3 residuals maintained almost zero at all tested conditions. In summary, O_3/DCM = 6 was the optimal conditions in this study both considered the economic and DCM degradation performance.

3.1.2 Other byproducts distribution. The generation of organic byproducts signifies incomplete degradation of VOCs. Due the Cl substitution, Cl-VOCs oxidation tends to produce Cl-containing organic byproducts, which might pose more serious

Table 1 The DCM conversion and the yield and selectivity of target products at 120 °C

Catalysts	Supports	DCM, con. (%)	CO_2, yid. (%)	CO_x, yid. (%)	HCl, sel. (%)	Cl_2, sel. (%)
M/A-I	γ-Al_2O_3	96.44	27.83	96.36	13.93	54.74
M/A-II	Nano γ-Al_2O_3	97.69	39.18	97.31	11.58	51.02
M/T	TiO_2	91.89	22.62	91.31	54.82	22.55
M/Z-I	ZrO_2	90.21	19.13	89.67	49.51	29.50
M/Z-II	Nano ZrO_2	92.58	24.95	91.27	46.89	31.64

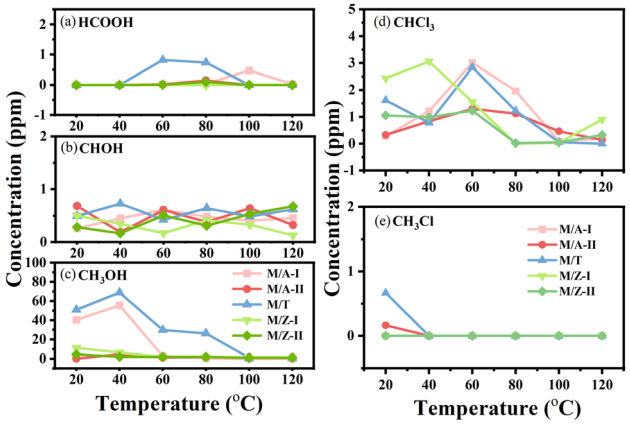

Fig. 3 Concentration curves of non-chlorinated (a)–(c) and chlorinated (d) and (e) organic by-products of DCM degradation over different catalysts with the function of temperature.

hazards. An FTIR analyzer was used to fully comprehend the distribution of these byproducts during the catalytic ozonation of DCM. Fig. 3(a)–(c) shows the concentrations of the three main non-chlorinated organic compounds with a function of temperature. Both CHOH and HCOOH were below 1 ppm. Comparatively, CH_3OH was the predominant byproduct of DCM degradation below 80 °C, which should originate from hydrodechlorination and oxygenation of DCM.[36] Similar to the first step of the DCE reaction mechanism on Mn/ZSM-5-27, CH_3OH was most likely produced by –OH species replacing the chlorine atom of DCM, and the alcohol species gradually decreased with increasing temperature.[36] Afterwards, under the oxidation of reactive oxygen species and O_3 and its decomposition products on the catalyst surface, CH_3OH was first converted to intermediate products such as formaldehyde (or carbonxylic-type species[2]) and formic acid (or R–COO^-),[33] and then formed CO_x by further oxidation. Apparently, all the four catalysts produced higher CH_3OH concentrations than those on M/A-II. On M/A-I and M/T, the CH_3OH concentration was higher at 20–40 °C, but dropped with increasing temperature, accompanied by a rapid rebound of DCM conversion (Fig. 2(a)). This phenomenon may be caused by the accumulation of continuously generated CH_3OH with high boiling point (64.7 °C) on the catalysts, which competes with the degradation of DCM. For M/Z-I and M/Z-II, although the concentration of CH_3OH was less than 10 ppm and declined to ~1 ppm at 60 °C, but the DCM conversion rebounded until 80 °C (Fig. 2(a)). The decreasing CO yields in Fig. 2(b) together with the increase in CH_3OH suggested a weaker recovery ability of M/Z-I and M/Z-II from the effects of CH_3OH.

Fig. 3(d) and (e) presents the dominant chlorinated organic byproducts, *i.e.*, $CHCl_3$ and CH_3Cl. Obviously, $CHCl_3$ is higher than CH_3Cl but all less than 3 ppm, which is consistent with the results of catalytic ozonation of chlorobenzene,[32] but contrary to the previous catalytic oxidation.[37] This may be related to the dissimilarity between the degradation mechanism of DCM catalytic ozonation and catalytic oxidation. The minimal byproducts on M/A-II suggested higher selectivity for the target product. In contrast, M/A-I and M/T possessed not only large amounts of CH_3OH, but higher concentrations of $CHCl_3$. In sum, the above byproducts reduced to *ca.* 1 ppm on the five catalysts when the temperature >100 °C.

3.2 Stability of DCM ozonation on M/A-II at 120 °C and 20 °C

As mentioned above, M/A-II not only attained such high DCM conversion at 20–120 °C, but also produced negligible organic byproducts, which verifies its superiority in catalytic ozonation of DCM. To evaluate the stability at 120 °C, Fig. 4 demonstrates variations of multi-parameters with function of time. Clearly, DCM conversion maintained above 95% during a long-time test of about 300 minutes. Throughout the whole reaction process, no O_3 residue was measured in the exhausts at an accuracy 0.1 ppm, implying no risk of ozone contamination. Cl_2 was the main product should be related to the abundance of weakly acidic sites. As shown in Fig. 4(b), the CO_2 yield varies from around 35% to 40% and carbon equilibrium was achieved within the absolute value of 6% ratio of C_{in-out}.

Moreover, the redox performance of M/A-II at 20 °C was comparable to catalysts with complex preparation methods and even to catalysts doped noble metal for O_2 catalytic oxidation at about 280 °C.[14,18] As shown in Fig. S2,† the DCM conversion of about 80% at 20 °C was also stable for about 120 min. Interestingly, the Deacon reaction for Cl_2 formation typically required a higher temperature,[7] but Cl_2 selectivity still attained 60–70% with a low HCl selectivity, *ca.* <5%, which should attribute to the promotion effects from O_3. However, after 60 min, the byproduct CH_3OH emerged and continually rose, which might attribute to the accumulation of intermediates on catalyst surface. The simultaneous larger decrease of CO yield in Fig. S2(b)† also demonstrated that more CH_3OH was produced without further deep oxidation. Overall, the too low temperature is not favorable for desorption of the deposits and induced catalyst deactivation in redox ability.

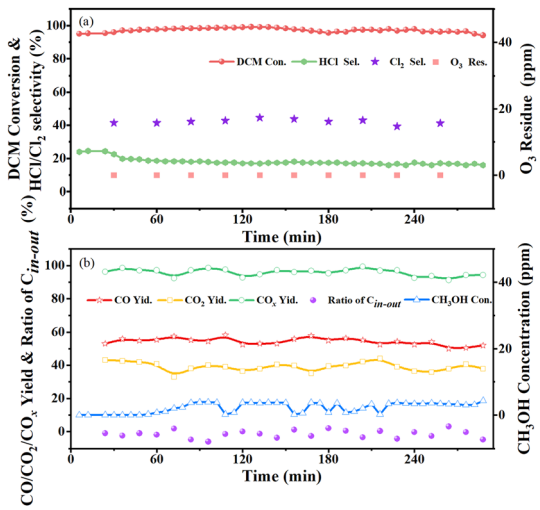

Fig. 4 Stability performance of the M/A-II with O_3/DCM = 6 at 120 °C. (Conditions: DCM initial concentration = 100 ppm; GHSV ≈ 30 000 h^{-1}).

3.3 Structure and surface properties

Fig. 5 presents the XRD patterns of synthesized catalysts and corresponding supports. The weakened intensity after Mn loading implied reduction in crystallization degree. The diffraction peaks of MnO_2 (PDF# 24-0735) and Mn_2O_3 (PDF# 41-1442)[31] could be hardly observed, indicating highly dispersion. ESD mapping images of metallic elements (Al, Ti, Zr) of the supports and loaded elements Mn in Fig. S3(f)–(j)† also confirmed the uniform dispersion of the Mn loading. According to the TEM results, only Mn_2O_3 crystals were found on M/T in Fig. S4(d),† and the rest possessed only supported crystals but not MnO_x crystals, indicating that most of the MnO_x was in amorphous form. The ICE-OES results (Table 2) confirmed Mn loading content of ~4 wt% over these catalysts. In terms of supports, the XRD patterns of M/A-I and M/A-II were PDF# 04-0877 (ref. 38) corresponding to γ-Al_2O_3.[39] The TiO_2 support had both rutile and anatase phases, with high proportion of anatase phase. Both M/Z-I and M/Z-II were monoclinic ZrO_2 (PDF# 37-1484).[40]

The N_2 adsorption and desorption isotherms and pore size distribution curves of the five Mn-loaded catalysts are displayed in Fig. S5.† They all belong to type IV isotherms with H3-type hysteresis loops. The pore size for all these catalysts was mostly dispersed across 50 nm, representing the coexistence of mesoporous and macroporous characteristics, which could improve mass transfer properties and gas molecule diffusions.[41,42] The M/A-I and M/A-II had larger specific BET surface area and smaller pore size (55–65 nm). The large specific surface area enhanced the dispersion and exposure of active sites, explaining the high DCM conversion at low temperatures of both M/A-I and M/A-II. The narrowed difference in DCM conversion with increasing temperature on the five samples indicates that the specific surface area and pore size had limited influence on catalyst activity.

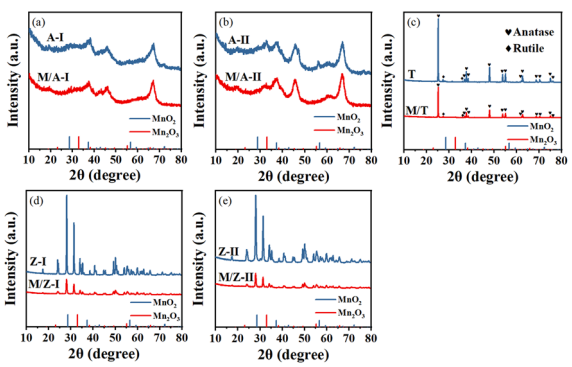

Fig. 5 XRD patterns of five synthesized Mn-loaded catalysts with corresponding supports.

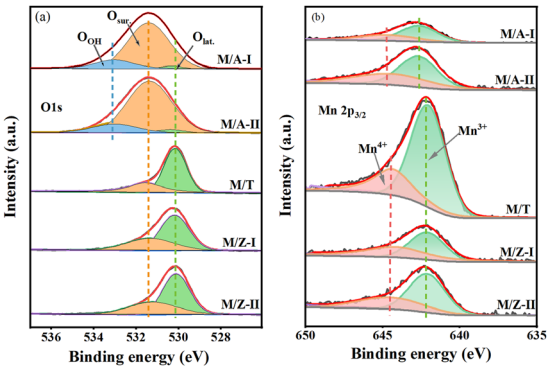

Fig. 6 XPS patterns of O 1s (a) and Mn $2p_{3/2}$ (b).

Fig. 6 presents the O 1s and Mn 2p XPS spectra with deconvolution results. The peaks of O 1s spectra were fitted to ~531.4 eV for surface adsorbed oxygen species (O^-, O_2^{2-}, denoted as $O_{sur.}$) and ~530.1 eV for lattice oxygen species (O^{2-}, denoted as $O_{lat.}$). The peaks at ~533.0 eV on M/A-I and M/A-II referred to adsorbed water species (–OH, denoted as O_{OH}). γ-Al_2O_3 supports (M/A-I and M/A-II) exhibited a much higher proportion of $O_{sur.}$ than ZrO_2 supports (M/Z-I and M/Z-II) (Table 3), which was advantageous for ozone decomposition and thus promoted catalytic ozonation.[31,33] The Mn $2p_{3/2}$ spectra possesses two typical peaks centralized at 642.1–642.6 eV and 644.1–644.9 eV, corresponding to Mn^{3+} and Mn^{4+}, respectively.[30] Since a higher percentage of Mn^{3+} implies a lower average oxidation state (AOS) and more oxygen vacancies, catalysts with nano-support (M/A-II and M/Z-II) possess better O_3 decomposition.[43] The highest percentage of $O_{sur.}$ was obtained for M/A-II, *ca.* 82.64%, which was consistent with the following O_2-TPD results. Besides, the effective promotion of high-density oxygen vacancies in the activated adsorption of surface oxygen species $O_{sur.}$ by O_2 molecules allows deep oxidation of VOCs.[44] In particular, $O_{sur.}$ was more critical at low temperatures.[24] Therefore, M/A-II attained the most effective performance in degrading DCM.

On the basis of the mechanism of catalytic ozonation of VOCs over Mn-based catalysts,[26,33,36,45] and byproducts measured by the flue gas analyzer (mentioned in section 3.1.2), we propose a possible mechanism for the catalytic ozonation of

Table 2 Specific surface area and pore structure parameters of the samples with loaded amounts of Mn

Catalyst	S_{BET} ($m^2\ g^{-1}$)	V_{Pore}[b] ($cm^3\ g^{-1}$)	Pore size[c] (nm)	Loading[d] (wt%)
M[a]/A-I	249.29	0.40	56.08	4.06
M/A-II	216.54	0.39	62.50	4.09
M/T	152.76	0.58	135.60	4.38
M/Z-I	27.89	0.21	287.95	4.70
M/Z-II	28.72	0.22	296.51	3.93

[a] M denotes the loaded MnO_x. [b] BJH desorption cumulative volume of pores. [c] BJH desorption average pore diameter. [d] Detected by ICP-OES.

Table 3 Binding energy and species distribution on O 1s and Mn $2p_{2/3}$

	O 1s					Mn $2p_{2/3}$		
Catalyst	O_{OH} (eV)	$O_{sur.}$ (eV)	$O_{lat.}$ (eV)	$O_{sur.}$ (%)	$O_{lat.}$ (%)	Mn^{3+} (eV)	Mn^{4+} (eV)	Mn^{3+}/Mn (%)
M/A-I	533.03	531.42	530.35	80.79	2.36	642.66	644.72	63.26
M/A-II	533.00	531.37	530.40	82.64	2.81	642.69	644.91	69.84
M/T	—	531.55	530.16	31.18	68.82	642.01	644.17	71.03
M/Z-I	—	531.34	530.19	36.66	63.34	642.10	644.16	50.31
M/Z-II	—	531.22	530.12	36.39	63.61	642.11	644.50	63.80

DCM. The activation reaction of O_3 and the electron transfer reaction that maintains the charge balance on the catalyst surface are the modes of involvement of Mn^{3+} and oxygen vacancies V_o. The electron transfer of Mn^{3+} or V_o (oxygen vacancy) activated O_3 to reactive oxygen species (HO_3^-/O_2^-) and continued the chain reaction of rapid conversion to O_2^-/OH^- (eqn (10)–(13)). To ensure the long-term cycling of the reaction, V_o was supplemented by decomposition of O_2^- or O_{lat} (eqn (14)). The released oxygen radicals were involved in the degradation of DCM. First, the chlorine atoms of DCM are replaced by –OH species to produce CH_3OH or intermediate species (O–CH_2Cl/O–CH_2–O) and HCl. In the presence of reactive oxygen species and O_3 with its activation products, they continue to be oxidized to intermediate products such as formaldehyde (or carbonyl-type species) and formic acid (or R–COO^-, CO_2^{3-}, *etc.*), followed by further oxidation to form CO_x. In addition, Mn^{4+} is restored to Mn^{3+} by an electron transfer reaction (eqn (15)), achieving the maintenance of charge balance on the catalyst surface and the replenishment of surface adsorbed oxygen.

$$Mn^{3+} + O_3/Mn^{3+} - OH + O_3 \rightarrow Mn^{4+} + O_{lat.} + O_2^-/Mn^{4+} + O_{lat.} + HO_3^- \quad (10)$$

$$3HO_3^- \rightarrow 3OH^- + 3O_2 \quad (11)$$

$$V_o + O_3 + 2e^- \rightarrow O_2 + O^{2-} \quad (12)$$

$$O_3 + O^{2-} \rightarrow O_2^- + O_2 + e^- \quad (13)$$

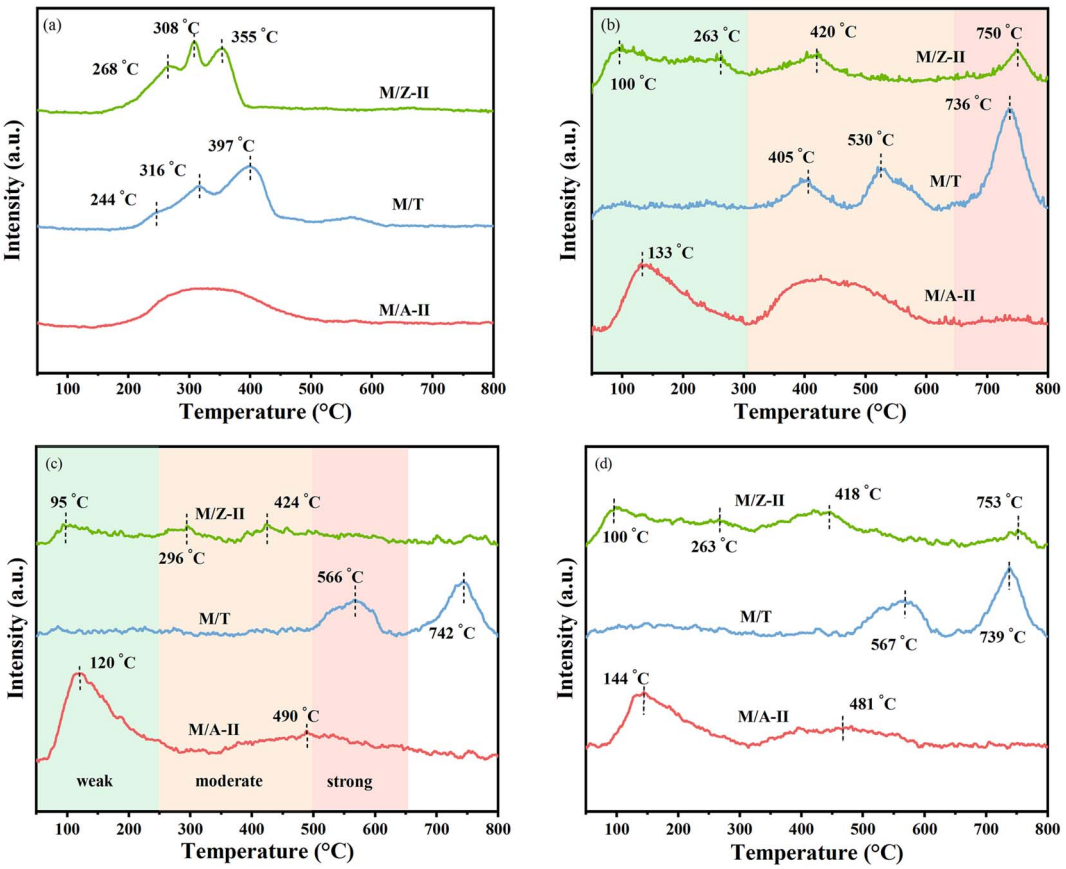

Fig. 7 (a) H_2-TPR, (b) O_2-TPD, (c) NH_3-TPD and (d) DCM-TPD profiles of M/Z-II, M/T and M/A-II.

$$O_2^- \rightarrow V_o + O_2 + e^- \quad (14)$$

$$Mn^{4+} + O_{lat.} + e^- \rightarrow Mn^{3+} + O_{sur.} \quad (15)$$

3.4 Redox ability, oxygen species mobility, and surface acidity

As the H_2-TPR profiles in Fig. 7(a), M/Z-II and M/T possess the large assembled peaks and the three peak tips correspond to the process of three valence changes of MnO_x.[30] The lower detected reduction temperatures in the latter two steps indicated better redox properties due to high dispersion. In addition, M/A-II merged the three reduction peaks into one peak with an increased percentage of peak area in the low temperature region. Interestingly, the H_2 uptake values (mmol g_{cat}^{-1}) estimated in Table 4 for M/T (0.45) > M/Z-II (0.43) > M/A-II (0.36) were in the reverse order of the DCM conversion. According to previous reports,[33,46] the lower reduction temperature rather than H_2 consumption amount of H_2-TPR curve was more directly related to the catalytic ozonation behavior.

Fig. 7(b) illustrates the O species distribution from O_2-TPD profiles, including surface adsorbed oxygen species (O_2, O^{2-} and O^-, –OH) at 100–300 °C, surface lattice oxygen (O_{ads}^{2-}) at 300–650 °C and bulk lattice oxygen (O^{2-}) above 650 °C.[20,30] According to quantitative estimates in Table 4, the quantitative O_2 desorption of M/A-II was the highest both in the low (6.27 a.u. g_{cat}^{-1}) and medium (8.13 a.u. g_{cat}^{-1}) temperature region, illustrating the high content and mobility of surface adsorbed oxygen species and surface lattice oxygen.[20,33] These characteristics promoted Deacon reaction,[47] resulting in the highest DCM conversion rate and strong resistance to chlorine-containing species. The distribution of surface acidity and acidic are crucial factors in catalytic degradation of VOCs. The NH_3-TPD profiles in Fig. 7(c) possess weak, medium, and strong acidity based on the temperature of the NH_3 desorption peak.[33,48] Table 4 further validates that the weak acid sites ratio decreased as the order: M/A-II > M/Z-II > M/T, which was associated with the breakage of C–Cl bonds,[33] thereby contributing to the highest activity on M/A-II. Additionally, the synthesis of HCl and Cl_2 was closely related to acidity and redox properties.[7,48–50] The stronger acidity of M/Z-II and M/T corresponded to their higher HCl selectivity. Although the acidity of M/A-II was weaker, it obviously had the largest peak area with a more abundant acid center. Moreover, the better low-temperature redox ability together with the promotion of O_3 could contribute to the improvement of Cl_2 selectivity, which was probably due to the Deacon reactions $2HCl + 1/2O_2 = Cl_2 + H_2O$ and $2HCl + O_3 = Cl_2 + H_2O$.[32]

The Py-IR profiles presented in Fig. S6† demonstrate that Lewis acid sites (1445 and 1610 cm^{-1}) predominated over Brønsted acid sites (1540 cm^{-1}) acid sites for all these catalysts, hence facilitating the breakage of the C–Cl bond and ozone decomposition.[18,30] As reported, the matched degree of acidity and redox ability within reaction temperature range was also important.[19] The abundant weak acidity of M/A-II could better match with the lower H_2 reduction temperature and higher O_2 mobility, thus explaining its excellent DCM degradation ability.

DCM adsorption is the first step for catalytic ozonation. The desorption properties of DCM over the catalyst were revealed using DCM as a probe molecule. As shown in Fig. 7(d), the DCM desorption below 200 °C decreased as the order: M/A-II > M/Z-II > M/T. M/T only possessed higher DCM desorption at 567 and 739 °C, demonstrating stronger adsorption affinity of DCM, which was disadvantageous for DCM conversion at such low temperature. Interestingly, the temperature points for M/A-II between DCM-TPD, O_2-TPD, and NH_3-TPD profiles were very close, contributing to its excellent performance at lower temperature.

3.5 Effect of SO_2 and H_2O

SO_2 and H_2O are inescapable in operational situations. Consequently, the effects of SO_2 and H_2O on DCM conversion and the selectivity of HCl and Cl_2 were investigated.

Fig. 8(a) presents the effect of H_2O alone on catalytic activity. After introduction of 1 vol% H_2O, DCM conversion rate gradually declined by 8% over the first 30 min and remained steady at 82%. Interestingly, the HCl selectivity was significantly increased by 20%, while Cl_2 selectivity decreased by the same amount. All these values returned back after removal of moisture. After feeding 3 vol% H_2O into the system, the DCM conversion rapidly decreased to 70%, showing a stronger competition impact. The HCl selectivity substantially rose to 70%, whereas the Cl_2 selectivity slightly declined to ~30%. Therefore, Cl equilibrium was thus attained by HCl and Cl_2, indicating the absence of significant organic chlorinated byproducts. In contrast, only 60–70% Cl equilibrium was achieved under dry conditions. Similarly, the recovery phenomena recurred after the removal of water. H_2O exerts a cleaning effect on the chlorine species (detailed in section 3.7) deposited on catalyst surface, hence limiting the synthesis of organic chlorinated byproducts.[20] Besides, H_2O could serve as a source of H for HCl production and retard the Deacon reaction.[51] On the whole, H_2O exhibited both positive and negative effects on

Table 4 Calculation parameters of H_2-TPR, O_2-TPD and NH_3-TPD

Catalysts	H_2 uptake (mmol g_{cat}^{-1})	O_2 desorption at low temperature (a.u. g_{cat}^{-1})	O_2 desorption at medium temperature (a.u. g_{cat}^{-1})	O_2 desorption at high temperature (a.u. g_{cat}^{-1})	Weak acid ratio (%)
M/A-II	0.36	6.27	8.13	1.01	54.10
M/T	0.45	1.51	5.11	5.53	12.42
M/Z-II	0.43	4.66	2.94	1.57	34.56

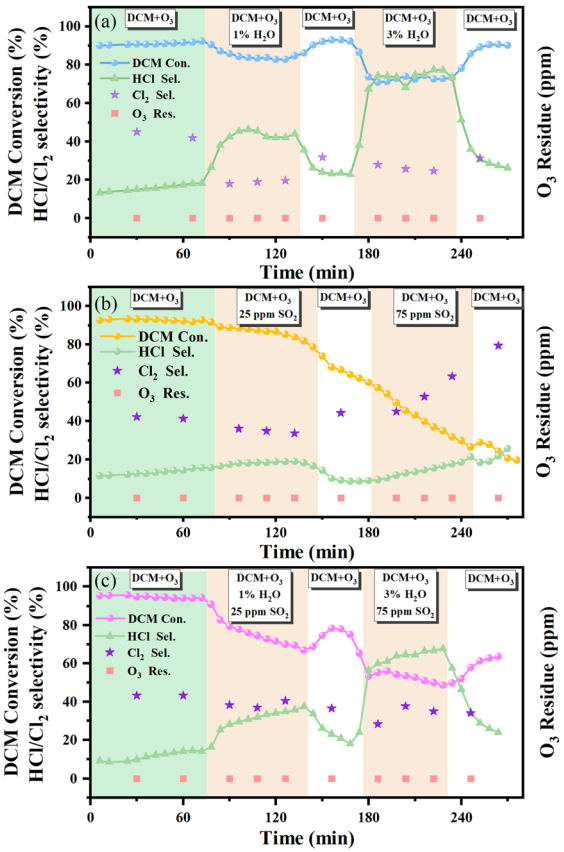

Fig. 8 Dynamic performance curves of DCM catalytic ozonation on the M/A-II with the effects of (a) water vapor, (b) SO_2 and (c) simultaneous presence of water vapor and SO_2. Water vapor content: 1 vol% and 3 vol%. SO_2 concentration: 25 ppm and 75 ppm. Initial DCM concentration: 100 ppm, O_3/DCM = 6.

catalytic ozonation of DCM. In the future, catalysts with a high hydrophobic performance and activation property should be developed to enlarge the positive effect and inhibit the negative effect.

The dynamic experimental curves of the individual effects of SO_2 are displayed in Fig. 8(b). Clearly, severe deactivation was detected in the SO_2 to DCM conversion process. Initially, only 2% drop in DCM conversion was observed and maintained for 30 min after the low concentration (25 ppm) of SO_2 was introduced into the reaction gas path. However, the curve dropped significantly after 30 min and the dropping rate gradually increased. More seriously, DCM conversion continued to fall at a slightly slower rate after removing SO_2. Next, higher concentrations (75 ppm) of SO_2 was added, accelerating the rate of decline until the DCM conversion reached ~20%. After 30 min of tolerance to low SO_2 concentrations, the active site on the M/A-II was progressively deactivated by the coverage of S(IV) species,[47] bisulfate species,[52] and trace sulfite species[53] (Fig. S7†). The deactivation of the sample was further confirmed by comparing the XPS images of Mn $2p_{3/2}$ (in Fig. S9(d) and (e)†), which showed a decrease in Mn^{3+} and Mn^{4+} and the presence of a small amount of Mn^{2+} (Table S1†). Lin *et al.* concluded that SO_2 could increase the yield of DCM and HCl during catalytic ozonation of chlorobenzene over MnO_x/Al_2O_3.[32] In combination with the present experiments, it was further confirmed that SO_2 could not enhance but rather inhibit catalytic ozonation of DCM. Surprisingly, the sharp enhancement of Cl_2 selectivity with decreasing catalyst activity could be attributed to the presence of several active sites of Deacon reaction still present. Furthermore, the emergence of CHOH, HCOOH and CH_3OH at the end of the test (Fig. S8†)[32] revealed the coverage of a large number of active sites by sulfides.[7,36] In summary, the M/A-II catalyst can endure brief exposure to low concentrations of SO_2. However, once the tolerable threshold was reached, the constant deposition of sulfate would cover the catalyst surface active sites and diminish its redox capacity. Future research on catalyst should focus on enhancing their capacity to transfer sulfate.

Fig. 8(c) depicts the change in catalyst performance resulting from simultaneous introduction of water vapor and SO_2. Following the addition of 1 vol% H_2O and 25 ppm SO_2, the DCM conversion declined rapidly by 10%. and kept falling to below 70%. During the first cut-off of H_2O and SO_2, the DCM conversion curve exhibited a parabolic shape. The first increase in DCM conversion is due to the re-exposure of H_2O adsorption sites that compete with DCM. The subsequent decrease was a result of the continued negative effect of SO_2 erosion. Surrounded by 1 vol% H_2O and 25 ppm SO_2 and higher concentrations of them, HCl production was increased to varying degrees, while Cl_2 remained almost unchanged. Thus, even with the high concentration of SO_2, the clearance of chlorine-containing species by H_2O helped to achieve the visible Cl equilibrium on M/A-II again. Interestingly, the DCM conversion remained at ~50% despite a pre-existing rapid reduction, during the feeding of 3 vol% H_2O and 75 ppm SO_2. In spite of the deposition of S species as well (Fig. S7†), the DCM conversion rose and stabilized at ~62% during the elimination high concentrations of SO_2 and H_2O. It could be inferred that the faster adsorption of water molecules shielded the active site on catalysts surface from sulfation, thus could postpone or even prevent the SO_2 erosion.

3.6 Further discussion for Cl balance of DCM decomposition

The present experiment achieved C equilibrium within the error range, but the final Cl-product was 30–40% different from the Cl content of the imported DCM (the detailed description and data are in the text of ESI and Fig. S10†). Herein, the surface Cl elements of the M/A-II catalyst after stability testing and the by-products undetected by the flue gas analyzer of the exhaust gas were analyzed. The deactivation induced by the deposition of chlorine-containing species during the catalytic oxidation of CVOCs tends to occur on Mn-loaded catalysts.[17,34,35] According to Fig. S9,† the abundant oxygen vacancies brought by ozone.[47] were unable to prevent the deposition of inorganic chlorine-containing species (*e.g.*, $MnCl_2$) and organic chlorine-containing species on the catalyst surface. But a deep oxidation of DCM at low temperatures was achieved, *i.e.*, the CO_x yield was very close to the DCM conversion in Fig. 2(b).[31,32]

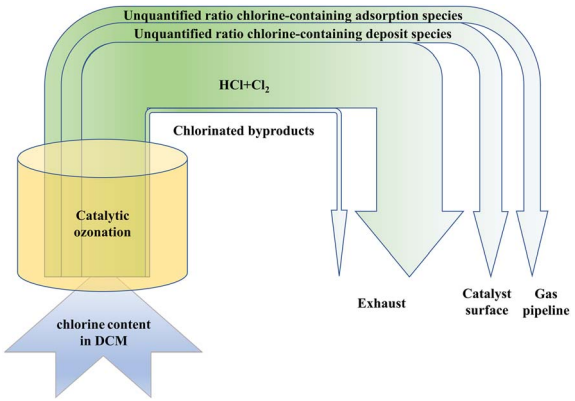

Fig. 9 A flow diagram of chlorine-containing species for DCM catalytic ozonation.

Simultaneously, the stability of the degraded DCM was substantially improved. As shown in Fig. S9(b),† more chlorine-containing species accumulate on the catalyst surface at 20 °C due to the slow transfer. Comparatively, fewer chlorine-containing species on the catalyst surface at 120 °C could stabilize the reaction for a longer time (Fig. 4 and S2†). Moreover, the clearance of chlorine-containing species (especially inorganic chlorine-containing species) deposited on the catalyst surface by H_2O verified the remarkable increase of HCl in section 3.5. Unexpectedly, multi-carbon byproducts CCl_4, $C_2H_4Cl_2$, and C_3H_5Cl (their generation mechanism could be referred to Fig. 6 in the review[49]) at the ppb level were detected in the off-gas (Fig. S11 and Table S2†) after stability reactions at both 20 °C and 120 °C. Tiny amounts of byproducts should be avoided in future studies. For instance, catalysts can be prepared using hydrothermal methods to improve product selectivity.[20,54] The absorption of the stainless steels tube for test[31,51] and the greening of the emulsion tube in the present experiment indicate that part of the chlorine-containing species was captured in the pipeline. A comprehensive analysis of the visible Cl equilibrium revealed the presence of four streams of chlorinated products (Fig. 9), including Cl_2 and HCl in the off-gas and adsorbed in the pipeline, the chlorine-containing species deposited on the catalyst surface and chlorinated byproducts all at the ppb level.

4. Conclusions

In conclusion, around 4 wt% Mn-loaded catalysts were synthesized on γ-Al_2O_3, nanoAl_2O_3, TiO_2, ZrO_2, and nanoZrO_2 supports using a simple impregnation method and evaluated for the catalytic ozonation of DCM. Firstly, the highly dispersed active species enabled all five catalysts to achieve more than 90% DCM conversion at 120 °C, mostly yielding of CO_x, Cl_2 and HCl. Among them, M/A-II exhibited the maximum DCM conversion and CO_2 yield with almost little byproduct. The larger specific surface area and multi-scale pores of M/A-II favored the degradation of DCM to some extent. In addition to the XPS pattern and O_2-TPD curve analyses, the facilitation of O_3 decomposition by Mn^{3+} and the promotion and enhancement of the Deacon reaction and chlorine species resistance by surface oxygen species also explained the best performance of M/A-II. Secondly, an increase in O_3 input (*i.e.*, an increase in the O_3/DCM ratio) an improved DCM conversion and a reduced byproduct at 120 °C. The optimal ratio of O_3/DCM was selected to be 6 at 120 °C, considering the economic and degradation effects. Strikingly, when the O_3/DCM ratio was 6, M/A-II maintained over 95% of the DCM degradation rate at 120 °C for about 300 min and 80% of the DCM degradation rate at 20 °C for approximately 120 min. Based on the results of H_2-TPR, NH_3-TPD and DCM-TPD, a good match between the superior DCM low temperature desorption performance, more surface weak acid sites and lower reduction temperature allowed for excellent DCM conversion even at lower temperatures. This provides an effective reference for the design of DCM degradation catalysts under moderate conditions. Thirdly, when the H_2O and SO_2 concentrations increased, deactivation on M/A-II intensified. The reversible deactivation caused by H_2O also cleaned up the chlorine-containing species (mainly inorganic chlorine-containing species) deposited on the catalyst surface, thus enhancing the HCl selectivity and achieving a visible Cl equilibrium. M/A-II can tolerate a low concentration of SO_2 briefly. Nevertheless, once the tolerance threshold he for S species deposition on the surface is reached, the catalyst deactivated irreversibly. The competitive adsorption of H_2O in the presence of both SO_2 and H_2O was a protection of the active site and retarded the deposition of S species. Finally, there are two reasons for the difficulties in achieving visible Cl ideal equilibrium (DCM with both HCl and Cl_2) for DCM degradation. First, the accumulation of chlorine-containing species on the catalyst surface. Second, the chlorine-containing adsorbed in the stainless steel and emulsion tubes.

Conflicts of interest

There are no conflicts to declare.

Acknowledgements

This research was financially supported by the National Natural Science Foundation of China [52125605] and the Fundamental Research Funds for the Central Universities [2022ZFJH004].

References

1 Y. Jing, Y. Wang, S. Furukawa, J. Xia, C. Sun, M. J. Hulsey, H. Wang, Y. Guo, X. Liu and N. Yan, *Angew. Chem., Int. Ed. Engl.*, 2021, **60**, 5527–5535.
2 X. Chen, S. Song, H. Li, G. Gozaydin and N. Yan, *Acc. Chem. Res.*, 2021, **54**, 1711–1722.
3 B. Huang, C. Lei, C. Wei and G. Zeng, *Environ. Int.*, 2014, **71**, 118–138.
4 S. N. Uang, T. S. Shih, C. H. Chang, S. M. Chang, C. J. Tsai and C. G. Deshpande, *Sci. Total Environ.*, 2006, **356**, 38–44.
5 N. Cheng, D. Jing, C. Zhang, Z. Chen, W. Li, S. Li and Q. Wang, *Sci. Total Environ.*, 2021, **752**, 141899.

6 Y. Ma, S. Fu, S. Gao, S. Zhang, X. Che, Q. Wang and Z. Jiao, *Environ. Pollut.*, 2021, **291**, 118253.
7 F. Lin, L. Xiang, Z. Zhang, N. Li, B. Yan, C. He, Z. Hao and G. Chen, *Crit. Rev. Environ. Sci. Technol.*, 2020, **52**, 311–355.
8 X. Liu, L. Chen, T. Zhu and R. Ning, *J. Hazard. Mater.*, 2019, **363**, 90–98.
9 H. Dai, S. Jing, H. Wang, Y. Ma, L. Li, W. Song and H. Kan, *Sci. Total Environ.*, 2017, **577**, 73–83.
10 R. W. Murdoch, G. Chen, F. Kara Murdoch, E. E. Mack, M. I. Villalobos Solis, R. L. Hettich and F. E. Loffler, *Global Change Biol.*, 2022, **28**, 2396–2412.
11 S. Pitkäaho, T. Nevanperä, L. Matejova, S. Ojala and R. L. Keiski, *Appl. Catal., B*, 2013, **138–139**, 33–42.
12 Q.-Y. Chen, N. Li, M.-F. Luo and J.-Q. Lu, *Appl. Catal., B*, 2012, **127**, 159–166.
13 Q. Ying, Y. Liu, H. Li, Y. Zhang and Z. Wu, *J. Colloid Interface Sci.*, 2022, **605**, 537–546.
14 J. Zhao, W. Xi, C. Tu, Q. Dai and X. Wang, *Appl. Catal., B*, 2020, **263**, 118237.
15 C. Zheng, H. Li, Y. Yang, S. Zhang, X. Yu, Q. Xin, S. Liu and X. Gao, *Proc. Combust. Inst.*, 2021, **38**, 6461–6471.
16 W. Ouyang, Y. Zhou, X. Fei, Y. Bai, H. Wang and Z. Wu, *J. Environ. Sci.*, 2022, **111**, 175–184.
17 L. Wang, G. Li, P. Wu, K. Shen, Y. Zhang, S. Zhang and R. Xiao, *Chem. Eng. Sci.*, 2021, **234**, 116405.
18 S. Cao, H. Wang, F. Yu, M. Shi, S. Chen, X. Weng, Y. Liu and Z. Wu, *J. Colloid Interface Sci.*, 2016, **463**, 233–241.
19 X. Fei, S. Cao, W. Ouyang, Y. Wen, H. Wang and Z. Wu, *Chem. Eng. J.*, 2020, **387**, 123411.
20 X. Feng, M. Tian, C. He, L. Li, J. W. Shi, Y. Yu and J. Cheng, *Appl. Catal., B*, 2020, **264**, 118493.
21 Y. Wang, A.-P. Jia, M.-F. Luo and J.-Q. Lu, *Appl. Catal., B*, 2015, **165**, 477–486.
22 H. Xia, H. Zhang, J. Wu, G. Chen, W. Sun, S. Shao, Q. Dai and X. Wang, *Appl. Catal., A*, 2021, **616**, 118094.
23 B. Zhou, X. Zhang, Y. Wang, J. Xie, K. Xi, Y. Zhou and H. Lu, *J. Environ. Sci.*, 2019, **84**, 59–68.
24 J. Kim, J. E. Lee, H. W. Lee, J. K. Jeon, J. Song, S. C. Jung, Y. F. Tsang and Y. K. Park, *J. Hazard. Mater.*, 2020, **397**, 122577.
25 H. C. Wang, H. S. Liang and M. B. Chang, *J. Hazard. Mater.*, 2011, **186**, 1781–1787.
26 C. He, Y. Wang, Z. Li, Y. Huang, Y. Liao, D. Xia and S. Lee, *Environ. Sci. Technol.*, 2020, **54**, 12771–12783.
27 F. Lin, Z. Wang, Z. Zhang, Y. He, Y. Zhu, J. Shao, D. Yuan, G. Chen and K. Cen, *Chem. Eng. J.*, 2020, **382**, 123030.
28 Y. Zhang, M. Chen, Z. Zhang, Z. Jiang, W. Shangguan and H. Einaga, *Catal. Today*, 2019, **327**, 323–333.
29 H. Einaga, N. Maeda and Y. Teraoka, *Appl. Catal., B*, 2013, **142–143**, 406–413.
30 J. Shao, F. Lin, Z. Wang, P. Liu, H. Tang, Y. He and K. Cen, *Appl. Catal., B*, 2020, **266**, 118662.
31 G. Chen, Z. Wang, F. Lin, Z. Zhang, H. Yu, B. Yan and Z. Wang, *J. Hazard. Mater.*, 2020, **391**, 122218.
32 F. Lin, Z. Wang, Z. Zhang, L. Xiang, D. Yuan, B. Yan, Z. Wang and G. Chen, *Environ. Sci. Technol.*, 2021, **55**, 3341–3351.
33 L. Xiang, F. Lin, B. Cai, K. Wang, Z. Wang, B. Yan, G. Chen and C. He, *J. Hazard. Mater.*, 2022, **436**, 13379–13390.
34 X. Fei, W. Ouyang, Z. Gu, S. Cao, H. Wang, X. Weng and Z. Wu, *J. Hazard. Mater.*, 2021, **413**, 125327.
35 Z. El Assal, S. Ojala, M. Zbair, H. Echchtouki, T. Nevanperä, S. Pitkäaho, L. Pirault-Roy, M. Bensitel, R. Brahmi and R. L. Keiski, *J. Cleaner Prod.*, 2019, **228**, 814–823.
36 H. Wang, B. Peng, R. Zhang, H. Chen and Y. Wei, *Appl. Catal., B*, 2020, **276**, 118922.
37 Z. Zheng, Y. Yang, H. Li, Q. Xin, S. Zhang, Y. Liu, S. Liu, C. Zheng, H. Song and X. Gao, *Fuel*, 2020, **278**, 118207.
38 E. Fu, Y. Qiu, H. Lu, S. Wang, L. Liu, H. Feng, Y. Yang, Z. Wu, Y. Xie, F. Gong and R. Xiao, *Fuel Process. Technol.*, 2021, **221**, 106945.
39 F. L. Chan and A. Tanksale, *Appl. Catal., B*, 2016, **187**, 310–327.
40 S. Wang, J. Pu, J. Wu, H. Liu, H. Xu, X. Li and H. Wang, *ACS Omega*, 2020, **5**, 30139–30147.
41 Z.-Y. Yuan and B.-L. Su, *J. Mater. Chem.*, 2006, **16**, 663–677.
42 P. Adelhelm, Y. S. Hu, L. Chuenchom, M. Antonietti, B. M. Smarsly and J. Maier, *Adv. Mater.*, 2007, **19**, 4012–4017.
43 J. Jia, P. Zhang and L. Chen, *Appl. Catal., B*, 2016, **189**, 210–218.
44 X. Zhang, Y. Liu, J. Deng, X. Yu, Z. Han, K. Zhang and H. Dai, *Appl. Catal., B*, 2019, **257**, 117879.
45 Y. Zheng, K. Fu, Z. Yu, Y. Su, R. Han and Q. Liu, *J. Mater. Chem. A*, 2022, **10**, 14171–14186.
46 L. Long, J. Zhao, L. Yang, M. Fu, J. Wu, B. Huang and D. Ye, *Chin. J. Catal.*, 2011, **32**, 904–916.
47 Z. Zhang, J. Huang, H. Xia, Q. Dai, Y. Gu, Y. Lao and X. Wang, *J. Catal.*, 2018, **360**, 277–289.
48 Q. Dai, W. Wang, X. Wang and G. Lu, *Appl. Catal., B*, 2017, **203**, 31–42.
49 F. Lin, Z. Zhang, N. Li, B. Yan, C. He, Z. Hao and G. Chen, *Chem. Eng. J.*, 2021, **404**, 126534.
50 Z. Zhang, H. Xia, Q. Dai and X. Wang, *Appl. Catal., A*, 2018, **557**, 108–118.
51 P. Sun, W. Wang, X. Weng, X. Dai and Z. Wu, *Environ. Sci. Technol.*, 2018, **52**, 6438–6447.
52 J. Baltrusaitis, D. M. Cwiertny and V. H. Grassian, *Phys. Chem. Chem. Phys.*, 2007, **9**, 5542–5554.
53 M. Wahlqvist and A. Shchukarev, *J. Electron Spectrosc. Relat. Phenom.*, 2007, **156–158**, 310–314.
54 H. Yan, M. Zhao, X. Feng, S. Zhao, X. Zhou, S. Li, M. Zha, F. Meng, X. Chen, Y. Liu, D. Chen, N. Yan and C. Yang, *Angew. Chem., Int. Ed. Engl.*, 2022, **61**, e202116059.